PNAS RESEARCH ARTICLE | CELL BIOLOGY OPEN ACCESS

Lysosome-related organelles orchestrate guanine crystal formation in pigment cells

Anna Gorelick-Ashkenazi[a], Yuval Barzilay[a], Tali Lerer-Goldshtein[a], Tsviya Olender[a], Zohar Eyal[a], May Glaser[a], Yonatan Broder[b], Nadav Mishol[a], Rachael Deis[a], Merav Kedmi[c], and Dvir Gur[a,1]

Affiliations are included on p. 11.

Edited by Breandan N. Kennedy, University College Dublin, Dublin, Ireland; received September 2, 2025; accepted March 11, 2026 by Editorial Board Member Jeremy Nathans

Iridosomes, the guanine crystal-forming organelles of pigment-producing iridophores, are among the most versatile, visually striking yet mechanistically uncharacterized organelles in vertebrate biology. Lysosome-related organelles (LROs) support cell type–specific functions by adapting endolysosomal pathways for specialized roles. Here, we show that iridosomes represent a subtype of LROs. Using transcriptomic profiling of zebrafish iridophores, CRISPR-Cas9-mediated gene disruption, and cryogenic transmission electron microscopy, we define the molecular program underlying iridosome biogenesis. Iridosomes have evolved unique adaptations for crystal growth while retaining core features of other LROs. Key regulators, including Rab32a, Ap3m2, and Hps5, are essential for crystal formation, with gene knockouts causing reduced crystal number, altered morphology, and distinct maturation defects. We further identify hallmark LRO features in iridosomes, including intraluminal vesicles and pH-regulated developmental transitions. Cross-species transcriptomic analysis confirms that iridosomes share an LRO signature across vertebrates, including teleost fish and reptiles, suggesting ancient evolutionary origins. These findings establish iridosomes as crystalline LROs and as a model for investigating how cells construct structurally specialized organelles through coordinated trafficking and crystallization, with implications for LRO evolution and human disease.

lysosome related organelle | zebrafish | iridosome | guanine | crystals

Significance

To form patterns, coloration, communicate, and enable vision, many organisms utilize guanine crystals formed within iridosomes, specialized crystal-forming organelles. Yet the biogenesis and maturation of iridosomes have remained poorly understood. Using zebrafish larvae, as a tractable, optically transparent system, we show that iridosomes are a specialized type of lysosome-related organelle (LRO). By combining comparative genetic, live imaging, molecular, and imaging approaches, we identify the molecular machinery and pathways that control iridosome biogenesis across vertebrates. Our work reveals that iridosomes have evolved unique adaptations for crystal growth while sharing common features with other LROs. These findings establish iridosomes as an in vivo model for studying how cells construct highly specialized organelles, with implications for understanding LRO evolution and human-related diseases.

Iridosomes, the guanine crystal-forming organelles of neural crest-derived iridophores (1, 2), are among the most visually striking yet poorly characterized organelles in vertebrate biology (3, 4). These membrane-bound compartments generate structural color through tightly packed guanine crystals (2, 5–8), enabling camouflage, signaling, and pattern formation across a wide range of species, including fish, amphibians, reptiles, and crustaceans (9–21). Despite their broad functional relevance, the developmental origin, molecular regulation, and classification of iridosomes remain largely unresolved. In contrast, melanosomes, another class of pigment organelles in neural crest-derived melanophores, are well established as Lysosome-related organelles (LROs) and have served as a foundational model for organelle specialization (22–26). Iridosomes exhibit an extraordinary degree of control over crystal size, shape, and organization, surpassing current manmade capabilities and represent a compelling model for understanding how cells orchestrate crystal formation within membrane-bound organelles (6, 15, 27–29). Although prior studies have suggested that disruption of LRO-associated machinery, such as LYST and different BLOC2 components, can influence iridophores (3, 30) it has not been systematically examined whether iridosomes themselves constitute a distinct branch of the LRO family, nor which conserved trafficking and maturation pathways govern their biogenesis.

LROs are a diverse group of cell type–specific compartments derived from the endosomal-lysosomal system (31, 32). Despite their shared origin, LROs exhibit a remarkable diversity in structures, compositions, and functions reflecting the specialized needs of different cell types (33). For instance, melanosomes in pigment cells synthesize and store melanin for photoprotection (23, 24, 34, 35), platelet dense granules release pro-adhesive factors to support homeostasis (36), and Weibel-Palade bodies in endothelial cells store and secrete proteins vital for vascular health (37). Additionally, LROs play crucial roles in immune responses, such as the cytotoxic granules of natural killer cells and cytotoxic T lymphocytes that release effector proteins to target pathogens (38).

The biogenesis and maintenance of LROs are governed by a complex molecular network involving key regulators such as Rab GTPases, adaptor protein (AP) complexes, biogenesis of lysosome-related organelle complexes (BLOC), and vacuolar protein sorting (VPS)

The authors declare no competing interest.

This article is a PNAS Direct Submission. B.N.K. is a guest editor invited by the Editorial Board.

[1]To whom correspondence may be addressed. Email: Dvir.gur@weizmann.ac.il.

This article contains supporting information online at https://www.pnas.org/lookup/suppl/doi:10.1073/pnas.2524305123/-/DCSupplemental.

Published April 8, 2026.

machinery (39). Among these, Rab32 and Rab38 play pivotal roles in vesicular trafficking and cargo delivery, ensuring the specialized maturation of LROs (40–42). The BLOC complexes, BLOC-1, BLOC-2, and BLOC-3- interact with Rab GTPases to facilitate the targeted transport of specific cargoes to LROs (23, 43, 44). The AP complexes AP-1, AP-2, and AP-3, were shown to be involved in sorting proteins required for LRO maturation (45–48).

A common hallmark of many LROs is dynamic pH modulation during maturation. For instance, Weibel-Palade bodies, derived from the Trans-Golgi network, undergo acidification (49), while endosome-derived melanosomes are initially acidic and experience a pH increase as they mature (32, 50). Similarly, recent findings suggest that iridosomes, organelles responsible for the formation of guanine-based crystals, also undergo a pH shift from acidic to neutral during their maturation (51).

Defects in LRO formation or function are linked to several genetic disorders, including Hermansky-Pudlak syndrome (HPS) and Chediak–Higashi syndrome, which manifests in conditions such as albinism, immune dysfunction, and bleeding abnormalities due to defective LRO biogenesis in melanosomes, cytotoxic granules, and platelet granules (22, 52). The versatility of LROs lies in their ability to integrate endosomal and lysosomal components to create functionally specialized microenvironments within the cell (4, 31–33). Better understanding of LROs provides insight into how cells rewire standard trafficking pathways to serve highly specific physiological roles.

We used zebrafish (*Danio rerio*) larvae as a tractable model for iridosome development (19, 27, 28, 53), because hundreds of crystal-forming organelles arise rapidly in the eye and skin during early development, a process important for camouflage and visual function (20, 54, 55). Zebrafish external development and optical transparency provide a unique opportunity to study LRO biogenesis in vivo, enabling direct visualization of iridosome formation, maturation, and dynamics within intact developing tissues. Through a combination of transcriptomic profiling of isolated iridophores, genetic perturbations, cryogenic transmission electron microscopy (cryo-TEM), live imaging, and ultrastructural investigations, we dissect the cellular origin and molecular regulation of iridosome biogenesis. Our findings reveal that iridosomes are a specialized type of LRO. Specifically, we demonstrate the involvement of key regulators, including Rab GTPases, AP complexes, and HPS proteins, which collectively orchestrate the formation and maturation of these optically functional crystals. Beyond defining iridosomes as LROs, our study provides perspectives on how organelle identity is established within specific cell types, and how large numbers of complex organelles are rapidly assembled and matured during early vertebrate development.

To place our findings in a broader evolutionary framework, we performed a comprehensive metadata analysis of publicly available transcriptomic datasets from multiple species. This analysis revealed that iridosomes are conserved as LROs across a range of taxa, including other teleost fish such as medaka (*Oryzias latipes*) (17), as well as reptiles like the leopard gecko (*Eublepharis macularius*) (56). This cross-species conservation suggests that the molecular mechanisms uncovered in zebrafish are likely to represent fundamental principles of iridosome biogenesis, underscoring their evolutionary significance and raising the possibility of conserved roles for iridosomes in visual and pigmentation systems across vertebrates.

Results

Transcriptomic Profiling of Zebrafish Iridophores Reveals Key LRO Pathways in Iridosome Biogenesis. Zebrafish utilize the unique optical properties of guanine crystals for a range of functions. These crystals, distributed throughout their skin and eyes (Fig. 1*A*), play a crucial role in coloration and patterning, contributing to camouflage, acting as light barriers, and enhancing visual sensitivity, particularly in low-light environments (20, 54, 57–61). In the developing zebrafish eye, guanine crystal formation starts around ~48 h post fertilization (hpf) (51, 62), contributing to iris reflectivity that limits unfocused light from reaching the retina and enhances visual sensitivity under dim-light conditions (59, 63). As development proceeds, increasing numbers of crystal-filled iridophores populate the iris (Fig. 1 *B–E*). Within these iridophores, each guanine crystal forms inside a membrane-bound organelle (Fig. 1*B*), with numerous crystals typically assembling within hours. (Fig. 1 *F–J* and Movies S1 and S2).

To investigate the origin and biogenesis of crystal-forming iridosomes, we isolated iridophores from zebrafish larvae at 5 d post fertilization (dpf). Fluorescence-activated cell sorting (FACS) followed by transcriptomic analysis was used to compare iridophores to a general, heterogeneous population of cells (*SI Appendix*, Fig. S1). We identified 1,222 significantly upregulated genes specific to iridophores (Fig. 2*A*), including established iridophore marker genes such as *pnp4a, tfec, slc2a15a, gmps, gpnmb, and alx4a* (Fig. 2*B*) (57, 64–68). Functional enrichment analyses using Metascape (69) highlighted key pathways enriched in iridophores, particularly the pigment granule organization as well as different lysosome-related pathways (Fig. 2*C* and *SI Appendix*, Fig. S2*C*).

To elucidate the molecular mechanisms underlying iridosome biogenesis, we focused on the machinery and regulatory components implicated in LRO formation. Our transcriptomic analysis revealed an enrichment of over 30 known LRO regulators (23) that were upregulated in iridophores (Fig. 2 *D* and *E* and *SI Appendix*, Fig. S2*D*). These included members of the Rab GTPase family (such as *rab38*, *rab32*, and *rab5*) (39, 40), AP complexes including *ap3* and *ap2* subunits (72, 73), and multiple BLOC complexes components (particularly *bloc1s1* and *bloc1s4*) (39, 43). Additionally, we identified multiple HPS proteins (*hps1*, *hps3*, *hps4*, and *hps5*) (7, 22, 23, 39), as well as various subunits of vacuolar ATPase (V-ATPase) (74) and VPS-associated proteins (22, 39) (Fig. 2 *D* and *E* and *SI Appendix*, Fig. S2*A*).

To quantify the overall enrichment of LRO genes, we compared the expression of a consensus set of 27 LRO markers (22, 23, 30, 39, 41, 44, 75–78) in iridophore samples versus the control samples (*SI Appendix*, Fig. S2*B* and Table S1). These genes were chosen based on three different parameters: i) Canonical conserved genes across different model systems. ii) Are known and established LRO genes that are key components that facilitate melanosome biogenesis. iii) These genes are conserved and known to be expressed in zebrafish. Iridophores displayed a significantly elevated expression of LRO genes relative to the control samples (Student's t test, two tailed, unpaired, $P < 0.0001$) (Fig. 2*F* and *SI Appendix*, Fig. S2*B*), further indicating that the iridosomes within iridophores represent a class of LROs.

To quantify LRO enrichment, we compared expression of a curated set of 27 LRO marker genes (22, 23, 30, 39, 41, 44, 75–78) between sorted iridophore and control samples (*SI Appendix*, Fig. S2*B* and Table S1). The marker set was assembled using three criteria: i) genes repeatedly annotated as canonical LRO components across multiple model systems, ii) genes with demonstrated roles in melanosome/LRO biogenesis, and iii) genes with conserved, expressed zebrafish orthologs. Iridophores showed a robust and statistically significant elevation of this LRO gene set relative to the heterogeneous control population (two-tailed unpaired Student's t test, $P < 0.0001$) (Fig. 2*F* and *SI Appendix*, Fig. S1*B*), supporting the classification of iridosomes as LROs.

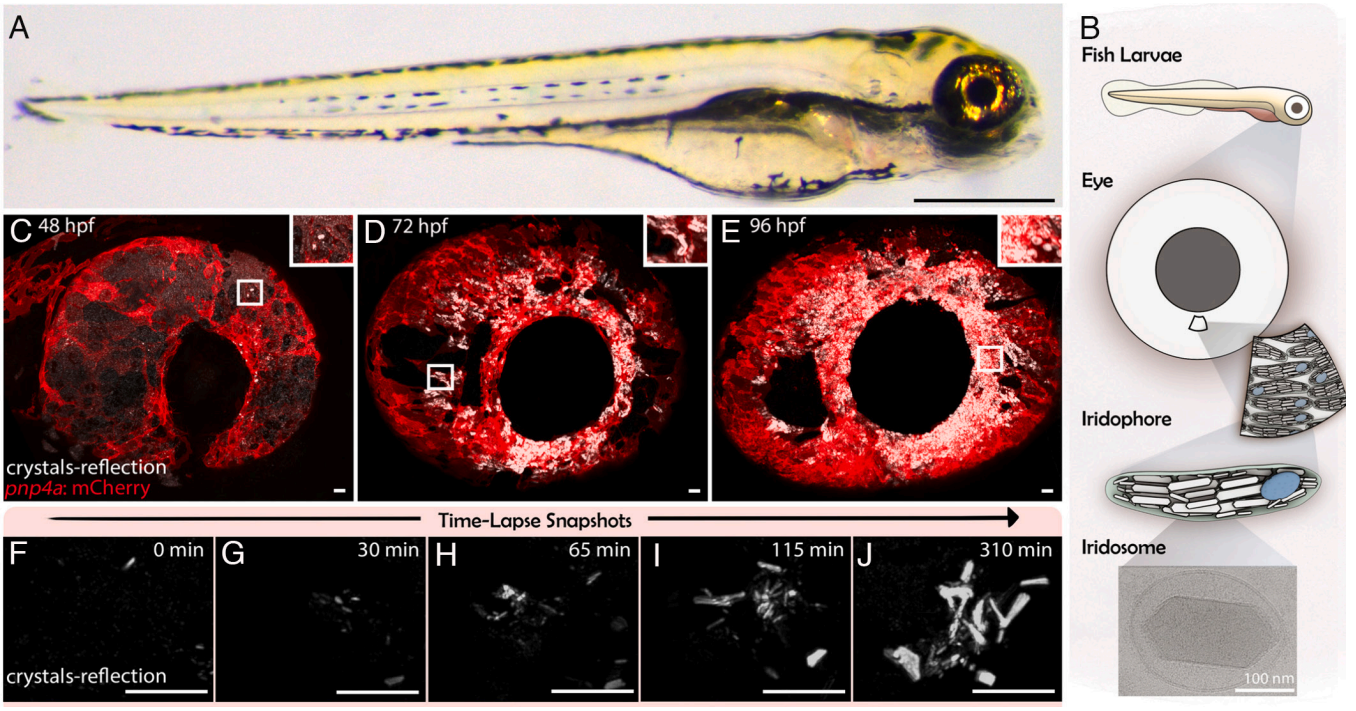

Fig. 1. Crystal formation dynamics and development in zebrafish eye iridophores. (*A*) Brightfield image of a 5 d post fertilization (dpf) zebrafish larva showing the highly reflective iris produced by guanine-based crystals in the eye. Scale bar, 500 μm. (*B*) Schematic of the spatial arrangement of iridophores in the larval eye and the guanine-containing iridosomes within them. *Bottom*: cryo-TEM image of a single membrane-bound iridosome containing a guanine crystal. (*C–E*) Maximum intensity projections (MIPs) from confocal imaging of *pnp4a*:PALM-mCherry (*pnp4a* is an established iridophore marker) (61) transgenic larvae at 48, 60, and 96 hpf, revealing the progressive differentiation of iridophores and the accumulation of intracellular crystals during development. Iridophore membranes are labeled in red, while guanine crystal reflectance is shown in white. *Insets* highlight higher magnification views. Scale bar, 10 μm. (*F–J*) Time-lapse confocal images of a single iridophore in the developing larval eye over 5 h. Initially, only a few guanine deposits are visible. As development proceeds, crystal number increases rapidly, reflecting active biogenesis of iridosomes during this developmental window. Scale bar, 10 μm.

To understand the functional relationships and connectivity among the upregulated LRO-related genes, we performed STRING analysis (70). Using the k-means algorithm, we clustered the network into three clusters showing a high degree of connectivity between the genes: one centered around VPS and Rab subunits, a second around BLOC and HPS proteins, and a third includes the AP complexes (Fig. 2*D*). The observed network architecture suggests coordinated regulatory framework likely associated with iridosome biogenesis, closely resembling mechanisms previously described for other LROs, including the closely related melanosomes (23).

In addition to known LRO regulators, our analysis revealed a subset of genes that may represent iridophore-specific adaptations to LRO biology. These include *rab20*, *rab3il1*, and *rabl6b* (*SI Appendix*, Fig. S2*A*), which were selectively upregulated in iridophores, and may reflect the functional specialization required for iridosomes.

Differential Roles of *rab32a* and *ap3m2* in Regulating Crystal Morphology and Abundance. Given the notable upregulation of LRO regulators in iridophores, we hypothesized that loss of function of specific LRO-associated genes would significantly impair iridosome biogenesis and guanine crystal formation. To test this, we used clustered regularly interspaced short palindromic repeats (CRISPR)-Cas9 genome editing to generate mutants targeting two key nodes identified in our network analysis (Fig. 2*D*). Specifically, we disrupted *rab32a*, a Rab GTPase known to regulate LRO maturation by coordinating trafficking and cargo delivery (40, 41, 44), and *ap3m2*, the μ3 (72, 73, 79–81) subunit of the AP complex AP-3, which mediates cargo sorting from endosomes to LROs (44). Both mutations resulted in premature stop codons predicted to produce nonfunctional proteins (Fig. 3 and *Materials and Methods*).

Both homozygous *rab32a*$^{-/-}$ and *ap3m2*$^{-/-}$ mutants showed a marked reduction in the number of crystals formed by iridophores (Fig. 3), without any detectable effect on overall larval development (*SI Appendix*, Fig. S3 *A* and *B*). A similar phenotype was observed in knockdown experiments using morpholinos (*SI Appendix*, Fig. S4), thereby further validating their roles in iridosome development. Notably, *ap3m2*$^{-/-}$ mutants showed a reduction in melanin pigmentation compared to WT siblings (*SI Appendix*, Fig. S5) as previously reported (80, 82, 83). In contrast, such a reduction was not observed in *rab32a*$^{-/-}$ mutants (*SI Appendix*, Fig. S5), potentially reflecting functional compensation in melanophores by Rab38, in agreement with previous reports (41, 84). The specific expression of *rab32a* and *ap3m2* genes in iridophores was also verified using a hybridization chain reaction (HCR) assay (*SI Appendix*, Fig. S4 *A* and *B*).

Interestingly, while the crystals formed by *ap3m2*$^{-/-}$ mutants were similar in morphology to those found in WT fish (Fig. 3 *A′* and *C′*), *rab32a*$^{-/-}$ mutants produced significantly shorter, with lower aspect ratio and more distorted crystals (Fig. 3*B′* and *SI Appendix*, Fig. S4*I*). These findings indicate that both Rab32a and Ap3m2 are important for iridosome biogenesis and crystal production. Rab32a appears to play a significant role in proper crystal shaping and structural integrity, whereas Ap3m2 is more generally involved in organelle biogenesis.

Severe Disruption of Iridosome Biogenesis and Crystal Formation in *hps5* Mutants. To further assess the role of LRO machinery in iridosome biogenesis, we investigated *Hps5*, a component of the BLOC-2 complex identified in the third node

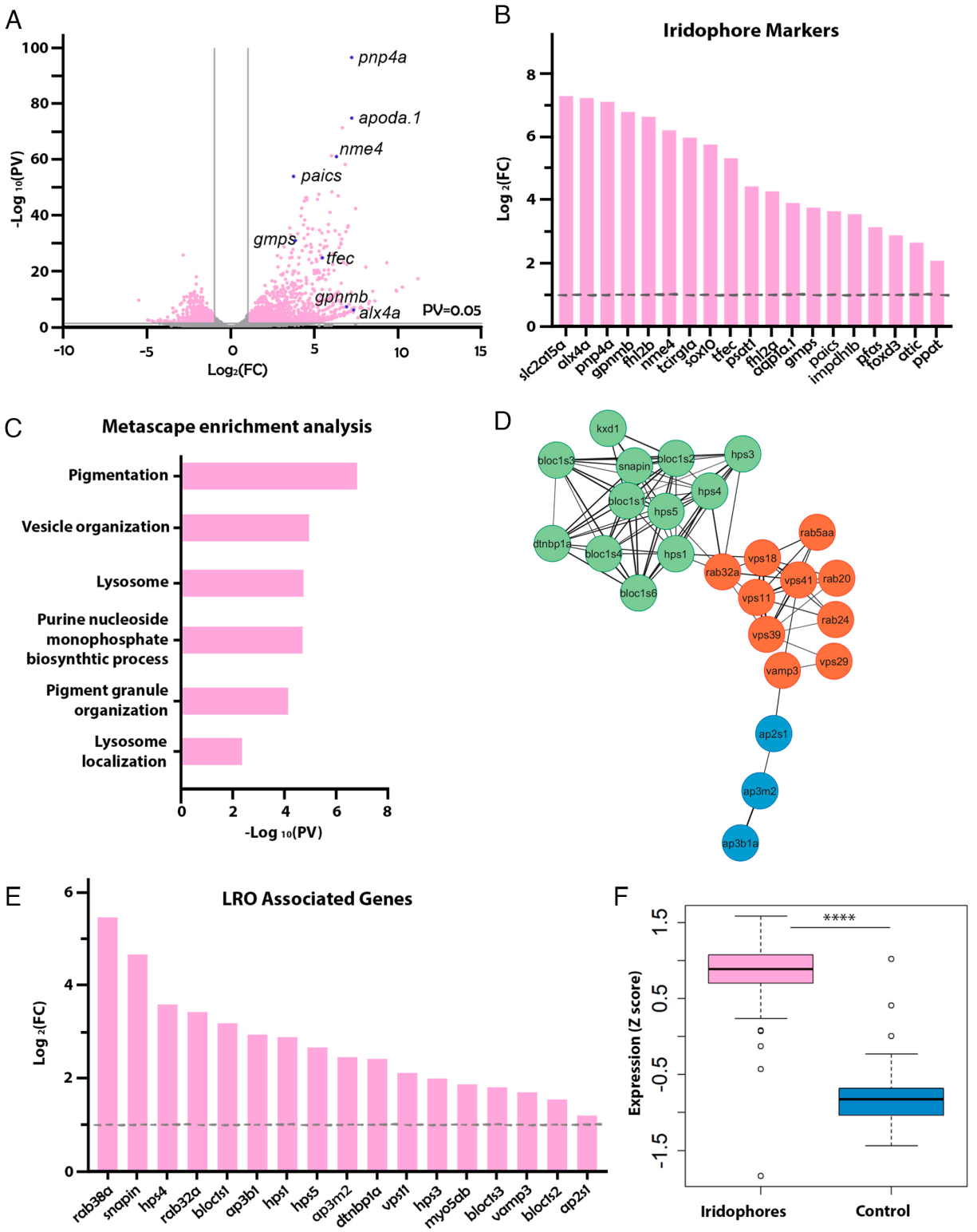

Fig. 2. Transcriptomic profiling of zebrafish iridophores reveals lysosome-related organelle (LRO) signatures. (*A*) Volcano plot showing differentially expressed genes between sorted iridophores (n = 3) and a heterogeneous control cell population (n = 3) from zebrafish larvae at 5 dpf. Genes with $P < 0.05$ and fold change >2 are highlighted in pink. Selected iridophore markers are highlighted by blue dots. (*B*) Bar plot illustrating elevated expression of canonical iridophore marker genes, including *pnp4a*, *tfec*, and *gmps*. (*C*) Gene pathways enrichment analysis performed using Metascape (69), showing significant upregulation of pathways related to lysosomes, vesicle organization, and pigment granule biogenesis (pink bars). (*D*) STRING (70) (https://string-db.org/) interaction network of LRO-associated genes significantly upregulated in iridophores. The network was clustered using the k-means algorithm into three distinct clusters: BLOC and HPS complexes (green), Rab and VPS proteins (red), and AP complexes (blue) and visualized using Cytoscape (71). (*E*) Bar graph showing the over expression levels of a consensus set of LRO marker genes in iridophores. (*F*) Distribution of the standardized LRO gene expression in iridophores vs. control cells. Iridophores show a significantly higher expression of LRO genes, supporting their classification as LRO-bearing cells. Significance determined by Student's test, two tailed, unpaired, ****$P < 0.0001$.

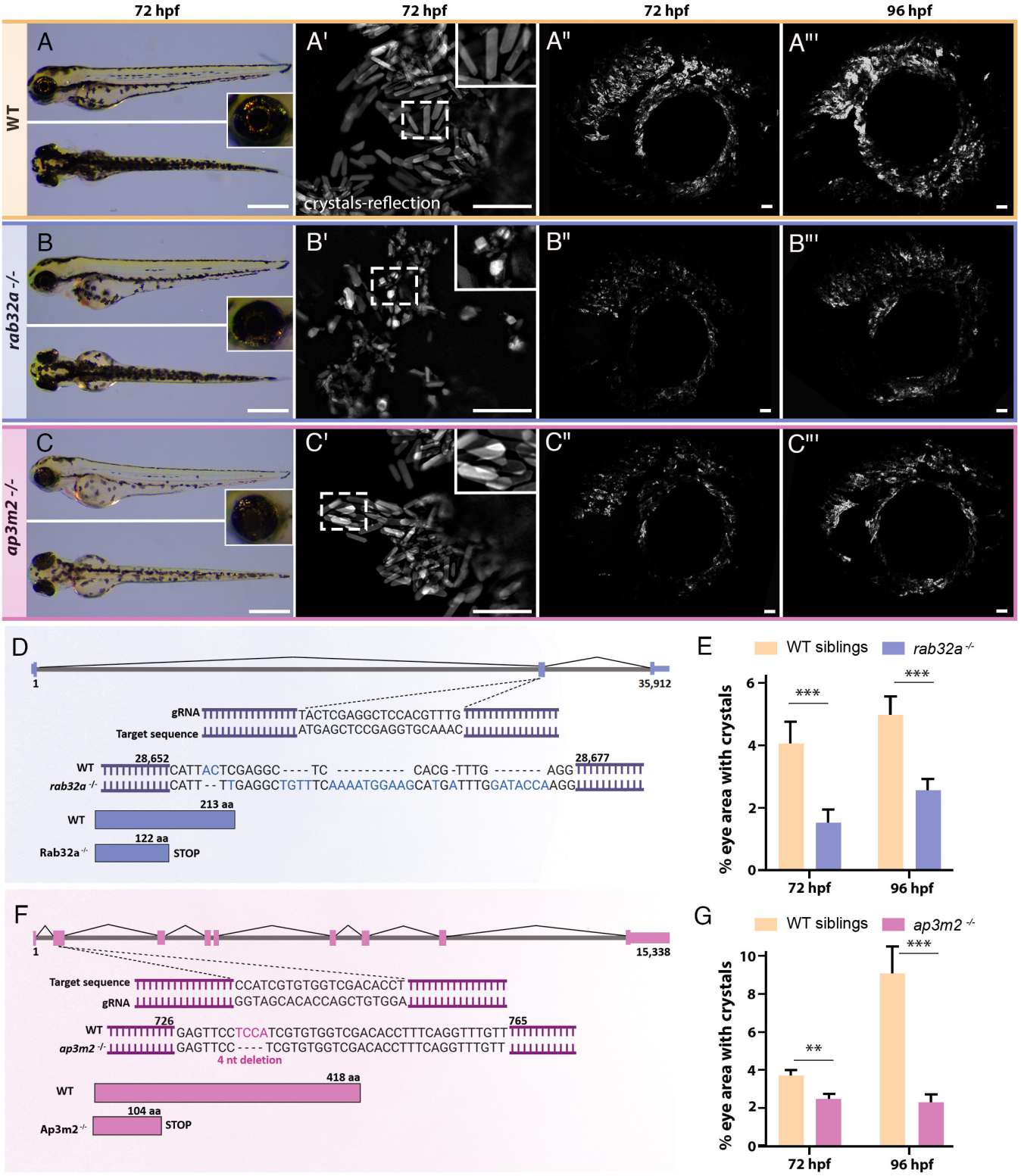

Fig. 3. Reduced crystal production in *rab32a* and *ap3m2* mutants, with distinct morphological alterations in *rab32a* mutants. (*A*–*C*) Brightfield images comparing wild type (WT) (*A*) *rab32a*$^{-/-}$ (*B*), and *ap3m2*$^{-/-}$ (*C*) larvae at 72 hpf. Insets highlight decreased iris reflectivity in *rab32a*$^{-/-}$ and *ap3m2*$^{-/-}$ mutants relative to WT. *ap3m2*$^{-/-}$ mutants also display reduced melanophore pigmentation. Scale bar, 500 μm. Reflectance imaging (*A′*–*C′*) and confocal MIPs of iridophores (*A″*–*C‴*) from WT and mutants at 72 and 96 hpf. Both mutants exhibit reduced crystal accumulation compared to WT. *Insets* in *A′* and *B′* highlight shorter and distorted crystals in *rab32a*$^{-/-}$ mutants, while *ap3m2*$^{-/-}$ mutants maintain WT-like crystal morphology. Scale bar, 10 μm. (*D* and *F*) Schematic of CRISPR-Cas9 targeting strategy for *rab32a* and *ap3m2*. *rab32a*$^{-/-}$ mutants harbor frameshift-inducing mutations leading to premature stop codons; *ap3m2*$^{-/-}$ mutants carry a 4-nt deletion resulting in truncation. Diagrams partially generated using BioRender.com. (*E* and *G*) Quantification of the percentage of eye area occupied by crystals in WT siblings versus mutants at 72 and 96 hpf. Data represent mean ± SEM. from ≥3 independent clutches. (*E*) 72 hpf: WT, n = 17; *rab32a*$^{-/-}$, n = 18. 96 hpf: WT, n = 18; *rab32a*$^{-/-}$, n = 21. (*G*) 72 hpf: WT, n = 21; *ap3m2*$^{-/-}$, n = 31. 96 hpf: WT, n = 18; *ap3m2*$^{-/-}$, n = 17. Significance determined by two-way ANOVA: ***$P < 0.001$; **$P < 0.01$; *$P < 0.05$. n = number of total larvae measured in different biological repeats.

of our network analysis (Fig. 4 *A*–*D*). In melanophores, BLOC-2 mediates trafficking of cargo such as TYRP1 from the endosome to stage III melanosomes (23, 30, 85). Strikingly, *hps5*$^{-/-}$ mutants exhibited a severely deficient capacity to form guanine crystals, with almost no crystals present in the eyes of 72 hpf larvae (Fig. 4 *B* and *B*′) without any detectable effect on overall larval development (*SI Appendix*, Fig. S3*C*). In parallel, and consistent with previous reports, *hps5* mutants also exhibited a pronounced reduction in melanin pigmentation (30) (*SI Appendix*, Fig. S5).

High magnification of crystals in 7 dpf mutant larvae revealed irregular-shaped assemblies (Fig. 4*B*″). The reduction in crystal formation and crystal shape impairment in the *hps5*$^{-/-}$mutant was far more pronounced compared to the other mutants we analyzed, suggesting that iridosome biogenesis and maturation are severely impaired in *hps5*$^{-/-}$ mutants.

The Presence of Intraluminal Vesicles (ILVs) Within Iridosomes Suggests an Endosomal Origin. After establishing the identity of iridosomes as LROs, we next examined their ultrastructural maturation and potential cellular origin using cryo-TEM. Early-stage iridosomes often contained multiple thin, developing crystals, whereas more mature iridosomes typically housed a single larger crystal (*SI Appendix*, Fig. S6), consistent with previous observations (27). In addition, we observed ILVs in a subset of iridosomes (*SI Appendix*, Fig. S6).

To determine how common ILVs are, we surveyed 81 iridosomes from 12 iridophores by cryo-TEM (iridosomes identified by crystals and/or internal characteristic fibers). ILVs were detected in 18 cases (22%) (*SI Appendix*, Fig. S6). When present, they ranged from small vesicles (~20 to 40 nm) to occasional much larger structures (96 ± 95 nm overall; up to several hundred nanometers). ILVs were less common in large, late-stage organelles, appearing only once among 10 iridosomes larger than 1,000 nm, consistent with ILVs being enriched at early stages of iridosome biogenesis. The presence of unusually large ILVs compared to other LRO systems may reflect structural specialization in iridosomes.

Because ILVs are a hallmark of multivesicular bodies and are commonly observed during the maturation of multiple LRO types, including melanosomes and cytotoxic granules (86–88), their presence within iridosomes supports an endosomal origin or an endosomal intermediate during iridosome formation and maturation.

Iridosomes are Conserved as LROs Across Diverse Vertebrate Lineages. To investigate whether the LRO identity of iridosomes is conserved beyond zebrafish, we analyzed publicly available single cell RNAseq datasets from other vertebrate species. Specifically, we calculated an "LRO score" for every iridophore cell from two additional organisms: the medaka (*O. latipes*) (17), a teleost related to zebrafish, and the leopard gecko (*E. macularius*) (56), a distantly related reptile (*SI Appendix*, Fig. S7 and Table S1). Using the same 27-gene LRO signature applied to zebrafish, we found that both medaka and gecko iridophores exhibited significantly elevated LRO scores compared to their respective general cell populations (Medaka: Student's *t* test, two tailed, unpaired, $P < 0.0001$; Gecko: Two-way ANOVA followed by Tukey analysis. $P < 0.0001$ for iridophores versus nonpigment cells and melanophores versus nonpigment cells. $P < 0.05$ for iridophores versus melanophores).These results further support the notion that the molecular machinery underlying iridosome biogenesis is deeply conserved across vertebrate taxa (*SI Appendix*, Fig. S7).

Discussion

Iridosomes as a Class of LRO and their Molecular Pathways. Our findings establish that iridosomes, the guanine crystal-bearing organelles of zebrafish iridophores, are members of the LRO family. By integrating transcriptomic profiling, gene perturbation, cryo-TEM, and comparative evolutionary analyses, we reveal that iridosome biogenesis depends on a similar molecular machinery that governs the formation of canonical LROs such as melanosomes, platelet dense granules, and Weibel-Palade bodies (31, 32) (Fig. 4*E*). These results place iridosomes within the expanding paradigm of LRO diversity and highlight their potential as a model for studying specialized organelle biogenesis.

Iridosomes align with LROs in several key respects. First, we show that iridophores express a suite of LRO-associated genes, including *rab32*, BLOC complex components, AP complexes such as AP3, and vacuolar sorting and proton pump machinery. Second, our functional studies demonstrate that disrupting key LRO regulators- Rab32a, Ap3m2, and Hps5, impairs crystal formation and/or organelle maturation. These defects recapitulate the phenotypes observed in canonical LRO systems, such as melanosome or dense granule disorders in HPS (22).

The phenotypes we observed for *rab32a* and *ap3m2* mutants show partial yet statistically significant reduction in crystal formation, a feature that is consistent with known redundancy and compensatory trafficking pathways in LRO biology (41, 48, 89). *Rab32a* mutants resulted in reduced crystal abundance rather than complete loss of iridosomes. This mirrors the situation in melanosomes, where Rab32 and Rab38 function redundantly to regulate cargo delivery, and single-gene disruptions often produce mild or partial pigmentation defects (41, 42). In zebrafish, teleost-specific gene duplication has further expanded this family with additional Rab38 paralogs (84), including Rab38b, and Rab38c, which are upregulated in iridophores, as well as Rab32 paralogs (Rab32a and Rab32b). Similarly, partial phenotypes are well documented for AP-3 deficiency in melanocytes, where parallel pathways-most notably AP-1-mediated trafficking, can partially substitute for AP-3 loss (82, 83, 89). It is therefore possible that functional compensation within the Rab32/38 and AP3/AP1 network buffers the loss of Rab32a and Ap3m2 in zebrafish iridophores as well.

Notably, the phenotypes of *rab32a* and *hps5* mutants suggest distinct contributions also to crystal morphology and organelle maturation, mirroring the specialized trafficking roles previously ascribed to these proteins in melanosomes (30, 41, 85, 90, 91). In melanosomes, Rab32a facilitate the delivery of cargo to maturing organelles through interactions with BLOC complexes (41, 44, 90). Their loss leads to mislocalization of cargo proteins and impaired pigment synthesis (41, 42, 90). Similarly, our findings suggest that Rab32a is required in iridophores to direct the trafficking of specific components necessary for proper crystal morphogenesis, such as guanine transporters, scaffold proteins, or pH-regulating channels, thus influencing crystal shape and organization.

Hps5 functions in the BLOC2 complex, which in melanophores is involved in transport from early endosomes to maturating melanosomes (23, 43, 44, 85, 91). Strikingly, *hps5* mutants had a severely deficient capacity to form guanine crystals, and almost no crystals were observed in the eyes of larvae. This reduction in crystal formation was much more pronounced than any of the other mutants we previously studied, suggesting that iridosome biogenesis is severely defective in these mutants.

Together, these results point to a functional division of labor among LRO regulators during iridosome development, in which

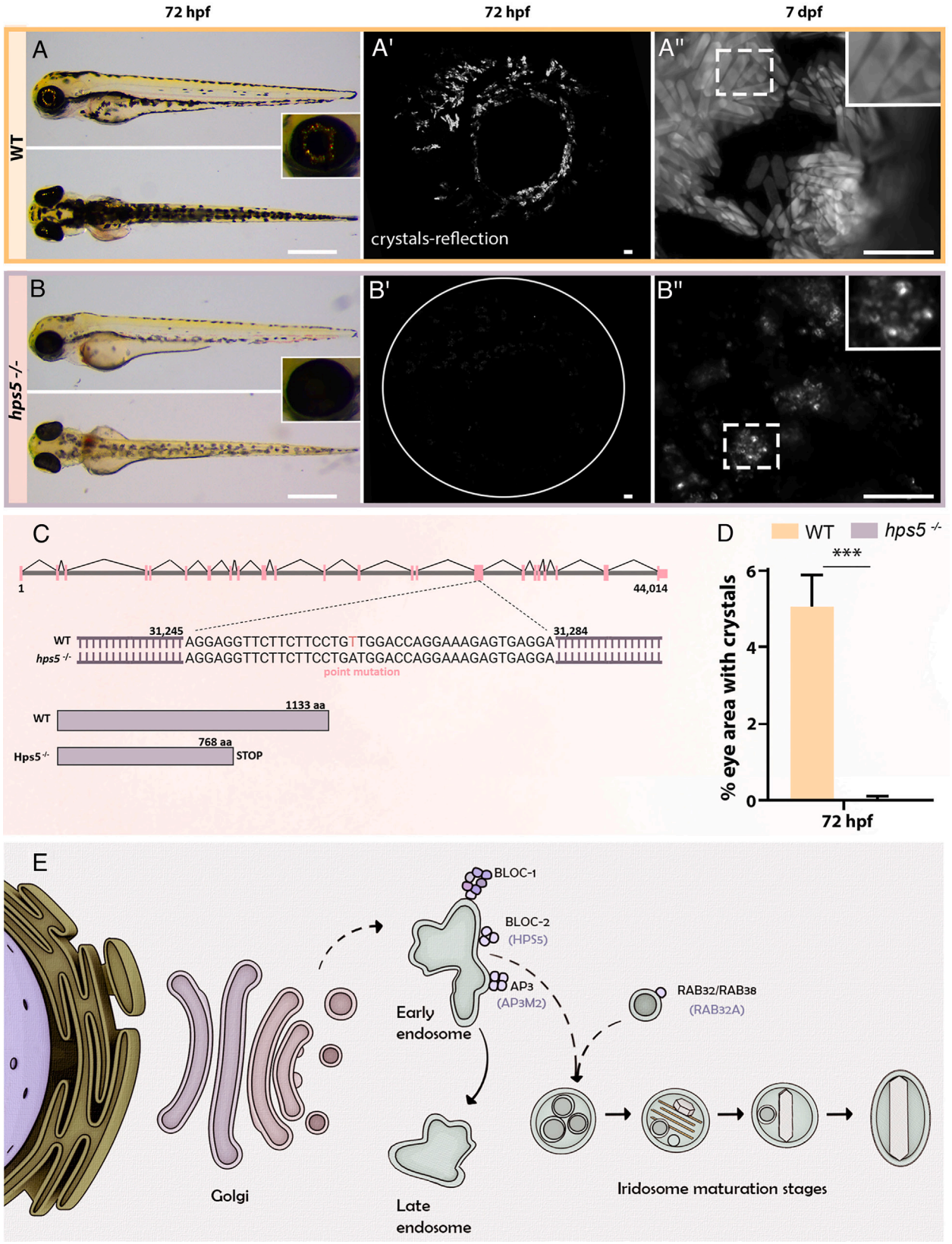

Fig. 4. Severe disruption of iridosome biogenesis and crystal formation in *hps5* mutants. (*A* and *B*) Brightfield images of WT (*A*) and *hps5*$^{-/-}$ (*B*) zebrafish larvae at 72 hpf. *Insets* show lack of reflective crystals in *hps5*$^{-/-}$ eyes and reduced melanophore pigmentation compared to WT. Scale bar, 500 μm. (*A′* and *B′*) Confocal MIPs of iridophores at 72 hpf and reflectance imaging at 7 dpf (*A″* and *B″*) showing near-complete absence of crystal formation in *hps5*$^{-/-}$ mutants. *Insets* in (*A″* and *B″*) highlight aberrant crystal aggregates in mutant iridophores. Scale bar, 10 μm. (*C*) Schematic of the *hps5* mutation, which introduces a premature stop codon resulting in a truncated protein. Illustration created in part using https://www.biorender.com/. (*D*) Quantification of the percentage of eye area containing crystals in WT and *hps5*$^{-/-}$ larvae at 72 hpf. Data represent mean ± SEM. from two clutches (WT, n = 10; *hps5*$^{-/-}$, n = 9). Significance assessed by two-way ANOVA: ***$P < 0.001$. n = number of total larvae measured in different biological repeats. (*E*) Proposed model illustrating the involvement of the endolysosomal pathway and the trans-Golgi network in iridosome biogenesis. LRO components implicated in crystal formation, including RAB32a, Ap3m2, and Hps5, are indicated in brackets.

certain components control organelle identity and cargo input, while others modulate the physical characteristics of the organelle's contents. This mechanistic architecture closely parallels with what has been described in melanosome biogenesis and further supports the classification of iridosomes as a specialized subtype of LROs.

Beyond the core LRO machinery shared with melanosomes and other systems, our transcriptomic analysis also identified several candidate regulators, *rab20*, *rab3il1*, and *rabl6b,* that may be unique to iridophores. These genes are not known to participate in melanosome biogenesis, suggesting that they may confer additional trafficking or regulatory capabilities tailored to the demands of guanine crystal formation. For instance, they could facilitate the transport of guanine precursors, modulate the luminal environment, or coordinate interactions between iridosomes and other organelles. Their selective enrichment highlights a possible layer of organelle-specific specialization within the broader LRO framework and raises the possibility that iridosomes have evolved dedicated molecular tools to support their crystalline function.

Endosomal Origin, PH Dynamics, and Intraluminal Vesicle Architecture. Beyond their molecular signature, iridosomes display defining structural features of endosomal origin. Cryo-TEM imaging revealed the presence of ILVs within maturing iridosomes, a hallmark of multivesicular intermediates observed in other LROs (25, 26). In melanosomes, for example, ILVs serve as organizing centers for premelanosome protein (PMEL) amyloid fibrils that template melanin deposition (92). By analogy, the ILVs observed in iridosomes may provide organizing centers for similar fibers or may serve for nucleation centers for guanine crystallization by themselves.

Another unifying feature of LROs is the modulation of their luminal pH, which regulates cargo condensation, enzymatic activity, and scaffold maturation (31, 37, 49). In melanosomes, lumen acidification is essential for tyrosinase activation and early pigment polymerization (50, 93). Our previous work demonstrating early iridosome (51) acidification, together with our current transcriptomic evidence for upregulated vacuolar-type H^+-ATPases (v-ATPases), suggests that iridosomes follow a similar developmental trajectory. We propose that nascent iridosomes are acidified to concentrate guanine precursors or control their solubility, with subsequent pH neutralization enabling crystal nucleation and elongation. The observation of internal, sheet-like or fibrillar structures in iridosomes from zebrafish and invertebrates (e.g., scallops, spiders) (27, 29, 51, 94) further supports a model in which LRO-derived scaffolds and acid–base transitions coordinate precise biomineralization within this specialized organelle.

Evolutionary Conservation and Expansion of the Functional Spectrum of LROs. The evolutionary conservation of iridosome identity as an LRO is further supported by our cross-species meta-analysis. We show that both the medaka and zebrafish, that are separated by approximately 200 million years of evolution, as well as reptiles, which diverged from teleost fish around 400 Mya (95), express orthologs of key LRO regulators in their iridophores. This suggests that iridosomes have ancient evolutionary roots, with their formation relying on a conserved regulatory network. This widespread conservation implies strong selective pressure to maintain crystalline optical organelles for light manipulation, camouflage, or signaling across environments and taxa.

Our results also broaden the functional scope of LROs to include crystal forming organelles, adding an additional dimension to the known functional diversity within this organelle class. While most LROs store pigments, small molecules, or secreted factors, iridosomes leverage LRO machinery to orchestrate spatially precise crystallization of purine metabolites. This finding reinforces the idea that LROs are not defined by their contents, but rather by their shared reliance on a specialized endolysosomal trafficking and maturation system tailored to cell-type-specific roles.

Iridophores as a Model for Organelle Morphogenesis and Bioinspired Design. Iridophores and their iridosomes offer an exceptional model for studying rapid organelle biogenesis, membrane-based crystal nucleation, and lumenal self-assembly processes. Given the transparency and tractability of the zebrafish model and the optical readouts provided by iridophores, future studies could leverage iridosomes to dissect how cells coordinate trafficking, pH regulation, and scaffold deposition to drive organelle specialization.

In summary, this study classifies iridosomes as LROs and reveals a conserved molecular framework for their biogenesis. These findings not only advance our understanding of pigment cell diversity and endomembrane specialization but also open avenues for investigating biomineralization and cellular optics through the lens of organelle biology.

Materials and Methods

Zebrafish Husbandry and Handling. Zebrafish (*D. rerio*) were housed at ~28 °C, 14 h light:10 h dark and fed with Artemia and flake food. Fish were maintained and fed following the standard protocols. Crosses were performed with at least three old adults. Embryos were kept in E3 zebrafish embryo medium at 28 °C until reaching the desired developmental stage. Lines that were used in this work are as follows: Et(Ola.Edar:GAL4,14xUAS:GFP)^{TDL358Et} (RRID: ZDB-FISH-150901-2380) (96), denominated ET358 for simplicity, Tg(*pnp4a*:PALM-mCherry)^{wprt10Tg} (RRID: ZDB-FISH-210414-18) (61), *hps5*$^{-/-}$ mutant [sa37981, European Zebrafish Resource Center (EZRC)] (RRID: ZDB-ALT-160601-5792) and AB (WT).

Cell Dissociation. Cell dissociation was carried out by customizing a protocol described previously (27, 28, 51). Briefly, hundreds of Tg(*pnp4a*:PALM-mCherry) positive 5 dpf larvae were anesthetized with Tricaine [0.1% MS-222 (Sigma)] and immersed in TrypLE Express (Invitrogen, 12604039). Fish were incubated at 37 °C and shaken at 200 rpm for 2 h, followed by mechanical disruption with vortex and pestles to further dissociate the cells. Cells were then strained through a 40 μM cell strainer with cold HL-15 buffer with 1 mM EDTA and centrifuged at 3,000 RCF for 5 min at 4 °C [HL-15 Buffer: Hank's Balanced salt solution 40% (Sigma H8264) and 60% Leibovitz's L-15 Medium (Gibco 21083-027)]. The pelleted cells were then resuspended in 10 mL of fresh cold HL-15 with 1 mM EDTA and then were incubated with Hoechst (H3570, Invitrogen) to mark the nuclei for 30 min before FACS.

FACS. Cell isolation was carried out by customizing a protocol described previously (27, 28, 51). Cells were isolated from Tg(*pnp4a*:PALM-mCherry) positive fish larvae and sorted via FACS. Cells were analyzed and sorted using a BD FACSAria™ III or V Cell Sorter with a 100 μM nozzle. Cells were illuminated using both 405 and 561 nm lasers. Cells were gated based on attributes to separate cells from each other as well as from cellular debris. Cellular debris was detected using forward, side scatter, and Hoescht signals to select against the smallest particles (1 mm or less). Cells were sorted and enriched based on i) Detection using 561 nm filters, corresponding to the *pnp4a*:PALM-mCherry signal and ii) The iridophores' high-intensity side scattering. For control samples, cells with low mCherry signal were collected.

Cells (~20,000 cells per sample) were collected directly into lysis buffer [Dynabeads® mRNA DIRECT™ Purification Kit (Ambion, 61012)]. After reaching ~20,000 cells each sample was vortexed, spun down and placed immediately on dry ice. The cell collection was performed in three biological replicates and stored in −80 °C before proceeding to next steps of sample preparation. For cryo-TEM, cells were collected into ice-cold HL-15 medium with 1% FBS and kept on ice until mounted on grids for downstream imaging.

RNA Isolation. Purification of RNA from sorted cells (~20,000 iridophores or general cell population) was done using Dynabeads® mRNA DIRECT™ Purification Kit (Ambion, 61012) according to manufacturer protocol. The purified RNA samples were frozen at −80 °C until the step of RNA-seq library preparation.

Bulk MARS-Seq Preparation. RNA-seq libraries were prepared at the Crown Genomics Institute of the Nancy and Stephen Grand Israel National Center for Personalized Medicine, Weizmann Institute of Science. A bulk adaptation of the MARS-Seq protocol (97, 98) was used to generate RNA-Seq libraries for expression profiling of iridophores and general control cell population. Briefly, RNA (all RNA amount purified from ~20,000 sorted cells) from each sample was barcoded during reverse transcription and pooled. Following Agencourt Ampure XP beads cleanup (Beckman Coulter), the pooled samples underwent second-strand synthesis and were linearly amplified by T7 in vitro transcription. The resulting RNA was fragmented and converted into a sequencing-ready library by tagging the samples with Illumina sequences during ligation, RT, and PCR. Libraries were quantified by Qubit and TapeStation as well as by qPCR as previously described (97, 98). For *D. rerio,* the housekeeping gene *actinb1* was selected for its relatively high and uniform expression (64) and was specifically calibrated for the MARS-Seq protocol. Sequencing was done on a NextSeq 500 using NextSeq High Output, 75 cycles, allocating 400 M reads in total (Illumina).

Bioinformatics Pipeline Methods

RNAseq Analysis. Data were analyzed with the User-friendly Transcriptome and Epigenome Analysis pipeline (UTAP) (v1.10.2) (99). The pipeline steps included fastq trimming using Cutadapt (DOI: 10.14806/ej.17.1.200) with the following parameters: -a AGATCGGAAGAGCACACGTCTGAACTCCAGTCAC -a "A" --times 2 -u 3 -u -3 -q 20 -m 25. The trimmed reads were then mapped to the danRer11 genome using STAR (v2.5.2b).

Quantification of raw read counts per gene was performed using the UCSC gene annotation. The quantification process involved marking read duplicates with an in-house UTAP script, followed by quantification using HTSeq-count (DOI: 10.1093/bioinformatics/btu638) in union mode. As MARseq is a 3′ protocol, the quantification was applied to a region that includes the 3′ 1,000 bp of each transcript and 100 bases downstream of the 3′ end was used for quantification.

Read count normalization and differential expression analysis were performed using DESeq2 (v1.36.1) (DOI: 10.1186/s13059-014-0550-8), with the betaPrior parameter set to TRUE. Genes with a log2 fold change (log2FC) > 1, an adjusted *P*-value (p.adj) < 0.05, and an average of >10 normalized read count in at least one of the compared conditions were considered differentially expressed.

The genes si:ch1073-75o15.4 and LOC100301575 are scaled outside of the plot therefore they were not included in the volcano plot.

scRNAseq Analysis.*Leopard Gecko.* The raw gene count matrix from the study (56) (GSE264342) was downloaded from GEO and reanalyzed using Seurat v5.1.0, and the same parameters and procedures as described in (56). Doublet detection was performed using scDblFinder (v1.18.0), and cells identified as doublets were excluded from further analysis. Low-quality cells were filtered out based on the following criteria: fewer than 1,000 detected genes, fewer than 2,000 UMIs, more than 9,000 detected genes, or more than 70,000 UMIs. To eliminate stressed or dying cells, we also removed cells with over 10% mitochondrial gene expression and over 30% ribosomal gene expression (63.3% of the cells passed these filters). Normalization was performed using Seurat's log-normalization method. Scaling was applied while regressing out cell cycle effects, using human cell cycle gene sets provided by Seurat. Following dimensionality reduction by PCA, we performed unsupervised clustering using Seurat's default Louvain algorithm at a resolution of 0.8 on a shared nearest neighbor graph constructed from the first 20 principal components. Nonlinear dimensional reduction for visualization was performed with the RunUMAP function using the first 20 principal components. Marker genes were identified using the FindAllMarkers function with the Wilcoxon rank-sum test, applying min.pct = 0.2 and logfc.threshold = 0.2. Genes with adjusted *P*-values < 0.05 (Bonferroni correction) were considered significant. Annotation of the different cell populations was based on the expression of the following genes derived from *SI Appendix*, Fig. S15 of (56): COL1A1, TWIST1, DSP, LOC129338255, EDAR, SOX2, TEK, PECAM1, MYOD1, TYRP1, OCA2, DCT, TYR, CORIN, SOX10, MITF, PMEL, LOC129342328, PAX7, LTK, TFEC, PNP, ALX4, and LOC129340104. Focusing on pigment cells, we used PNP expression as a marker for iridophores, OCA2 as a marker for melanophores. The annotation was further validated by querying the PanglaoDB database with the marker genes of each cluster, using the R package, enrichR (100).
LRO score of each cell was calculated using the AddModuleScore function of Seurat, and with the genes listed in the *SI Appendix*, Table S1. These are genes with a well-established function in LROs.
Medaka. Medaka scRNAseq data were available from the study of (17). LRO score was calculated using the AddModuleScore function of Seurat, and with the genes listed in *SI Appendix*, Table S1.

Bulk RNA-seq Deconvolution. Bulk RNA-seq deconvolution was performed using CIBERSORTx (101) with the Daniocell (102) dataset (108 to 120 hpf) as reference. Cell types represented by fewer than 100 cells, as well as cell types with an excessive number of features (Z-score > 1.96), were excluded to prevent disproportionate influence on downstream deconvolution. To reduce computation time, the signature matrix was computed using 500 randomly selected cells per cell type and the 15,000 most variable genes. This signature matrix was subsequently used for the deconvolution of the bulk RNA-seq samples.

Metascape Analysis. Gene pathways enrichment analysis for identifying upregulated biological processes for identified genes was done using a Metascape algorithm (69) (http://metascape.org). As a background for the analysis we used all genes that were detected in the data.

***rab32a* and *ap3m2* CRISPR Mutants.** The *rab32a* and *ap3m2* CRISPR mutants were generated as described previously (103). Briefly, trans-activating crispr RNAs (crRNAs) were designed for specific loci of the *rab32a* and *ap3m2* genes using the predesigned crRNAs dataset from Integrated DNA Technologies (IDT). Several crRNAs were tested for ribonucleoprotein (RNP) mutagenesis and were chosen considering where the start codon is located, as well as high on-target and low off-target scores. The most efficient crRNA tested was located on exon 2 of the *rab32a* and exon 2 of the *ap3m2* canonical transcripts, with target sequence
5′-CAAACGTGGAGCCTCGAGTA-3′ (Dr.Cas9.Rab32A.1.AA, IDT) and 5′-CCATCGTGTGGTCGACACCT-3′ (Dr.Cas9.AP3M2.1.AD, IDT) respectively. Each tested crRNA was separately annealed with an equal molar amount of tracrRNA (1072533, IDT) and diluted to 57 µM in Duplex buffer (11-01-03-01, IDT), generating the single guide RNA (sgRNA). The RNP mixes were assembled using Cas9 protein (Alt-R S.p. Cas9 Nuclease V3; 1081058, IDT; 61 µM stock) and a sgRNA, in equimolar amounts, generating a 28.5 µM RNP solution. One-cell-stage WT AB embryos were injected with 1 nL of each of the RNP mixes. To screen for the efficiency of RNP mutagenesis pools of 5 embryos of each RNP-injected condition were individually genotyped. Founder fish (F0) containing frameshift mutations were identified by genotyping

the resulting F1 progeny, resulting from outcrosses with WT AB fish. F1 progeny were genotyped and fish carrying identical mutations crossed to produce F2 generation that contained mutant, WT siblings, and heterozygous fish. F3 pure mutant line was raised after crossing F2 mutant fish.

The mutant lines that were generated: 1) *rab32a*$^{-/-}$ resulting in a series of genetic alternations (Fig. 3), leading to a truncated protein, resulting in 122 aa instead of 213 aa. 2) *ap3m2*$^{-/-}$ resulting in a 4 nt deletion (Fig. 3), leading to a truncated protein, resulting in 104 aa instead of 418 aa.

Genotyping. Genomic DNA from individual larvae, pool of larvae or adult after fin clipping, was extracted according to following protocol: samples were incubated in 100 µL 50 mM NaOH at 95 °C for 20 min then cooled in 4 °C for 2 min. 10 µL of Tris-HCL (pH 8) was added to each sample that was vortexed and centrifuged at 12,000 rcf for 2 min. This was followed by performing PCR with Red Load Taq Master mix (Larova) with primers surrounding the *rab32a* mutation region (forward, 5′-TTATGTCCCACGTCTAGGTCAG-3′; reverse, 5′-GCTTCGGCTTGACCTATTAC -3′) or with primers surrounding the *ap3m2* mutation region (forward, 5′-TGTAA GGATGCTGGCAGGTTG-3′; reverse, 5′-CCTGGCTACA GGCCTAATTA -3′). For genotyping of *hps5*$^{-/-}$ (sa37981, EZRC) adult fish and larvae the following primers were used surrounding the *hps5* mutation region in exon 16 (forward, 5′-TAGAGAGAGCACCCCCTGTTCCATC-3′; reverse, 5′- TACA GTAAACTCACCCAGCATGCCA -3′). The point mutation results in nonsense mutation leading to a truncated protein, resulting in 768 aa instead of 1,133 aa (Fig. 4). All PCR products were sent for sanger sequencing. Sequences were analyzed using Snapgene software.

Live Imaging. For imaging, live larvae were anesthetized with Tricaine and then mounted with 0.9% low-melting-point agarose (Sigma, A9414) on an imaging glass bottom dish (Cellvis, d35-14-1.5-n). Live imaging was carried out on inverted Zeiss LSM 980 or 900 confocal microscopes using X20, X40, or X63 lenses. Crystals were imaged with reflection. For time-lapse imaging, mounted larvae were covered with E3 medium with tricaine and placed inside a chamber with controlled 28 °C. Imaging was done up to 48 h. Images from each session were processed into a movie using the ImageJ software.

For confocal imaging quantifications, Z-stack images of the eye area with crystals (1.25 µm each slice, total 30 to 50 µm) were taken using X20 magnification lens. Whole larvae imaging for standard length (SL) (104) measurements were done using X2.5 lens.

For gross morphology images, larvae were anesthetized with Tricaine and placed in Methyl Cellulose and imaged with Leica M80. For melanophore imaging (*SI Appendix*, Fig. S5), larvae were kept under direct light for at least 15 min to promote optimal melanophore aggregation, then imaged under the same conditions for all genotypes.

For high-resolution images of the crystals (Fig. 3 *A′–C′* and Fig. 4 *A″* and *B″*), live larvae were mounted on glass slides and their eyes imaged with X100 lens using the Leica DM-6B upright microscope. The images were then analyzed using ImageJ for length and width measurements of individual crystals and the aspect ratio calculated for each crystal.

Plunging and cryo-TEM. As previously described (27, 28), sorted iridophore cells (3.5 µL) with 15 nm gold beads (1 µL) were applied to glow-discharged holey carbon R2/2 Cu 200 SiO_2 mesh grids (Quantifoil) coated with collagen, Type I, rat tail (EMD Millipore, 08-115) for cell adherence. The grids were blotted and vitrified by plunging into liquid ethane using a Leica EM GP automatic plunger at 4 °C and 90% humidity. Frozen grids were kept in liquid nitrogen until used. Data were collected on a Titan Krios TEM G3i (Thermo Fisher Scientific) equipped with a BioQuantum energy filter and a K3 direct electron detector (Gatan). Cryo-TEM images (*SI Appendix*, Fig. S6 and in Fig. 1) were taken at 300 kV with the K3 camera (counting mode) using Thermo Fisher Tomography software.

Quantification of ILVs. The iridosomes diameters, and the ILVs abundance and dimensions were quantified from cryo-TEM micrographs where the organelles were clearly resolved. All measurements were performed using the IMOD software (105). Data were collected from 12 iridophores, totaling 81 iridosomes. These quantitative analyses are presented in *SI Appendix*, Fig. S6.

HCR Fluorescence In Situ Hybridization (HCR) Assay. 5 dpf WT (AB) larvae were fixed in 4% PFA over night at 4 °C, washed 3× in PBT (Triton 0.1% in PBS) and transferred to 100% MeOH to be stored in −20 °C until further use.

For HCR assay, fixed larvae were washed twice in SSCTX2 and ~10 larvae per sample were incubated with 4 nM probe (*pnp4a* and *rab32a* or *ap3m2*, Molecular Instruments) in preheated hybridization buffer (2XSSCT,10% dextran sulfate, 10% formamide, Molecular Instruments) at 37 °C, overnight with agitation. Next samples were washed with preheated wash buffer (2XSSCT, 30% formamide, Molecular Instruments) for 30 min at 37 °C with agitation, then washed twice for 20 min in SSCTX5 at RT and incubated for 30 min in amplification buffer (5XSSCT,10% dextran sulfate, Molecular Instruments) at RT. Next, samples were incubated with appropriate snap-cooled hairpins (hairpins h1 and h2 (Molecular Instruments) 180 nM each) in amplification buffer overnight in the dark at RT, followed by washes with SSCTX5 (3× 20 min) at RT. The samples were then mounted and imaged using confocal microscopy for RNA localization in the larval eye.

Microinjection of Embryos With Morpholinos. One-cell-stage TDL358 or *pnp4a*:PALM-mCherry embryos were injected using standard procedures with a PV850 microinjector and M3301 Manual Micromanipulator (World Precision Instruments) that were used for microinjection. Gene knockdown experiments were performed using the following morpholino-modified antisense oligonucleotides (MO, Gene Tools):

rab32a, 5′ TGCCATGCTGCCAAAATGTCAGTTA 3′; AUG MO.

ap3m2, 5′ ACTAACAGAGATTACCTGTGATGGT 3′; Exon Junction MO.

control morpholino, 5′ CCTCTTACCTCAGTTACAATTT ATA 3′ (Gene Tools stock control).

Each oligonucleotide was diluted with ultrapure (Milli-Q) water to 1 mM and 1 to 2 pmol of MO was injected into one-cell-stage embryos. Embryos were left to develop at 28.5 °C until the desired stage and then live-imaged.

Reflectance and Fluorescence Coverage Quantification. For the quantification step done on confocal images, a custom graphical user interface application was developed. The application accepts images in the czi format and creates maximal intensity projections over the images, allowing for further processing and visualization. The application then performs an automatic object detection and segmentation step, followed by optional manual annotation, user-specified thresholding, and area to area calculation and output. In every step of the workflow the application allows visualization of

the dataset and of the segmentation. It was implemented in Python, utilizing OpenCV, PIL, Tkinter/CustomTkinter, Matplotlib, NumPy, and Pandas for image processing, visualization, and data management, and with aicspylibczi for handling czi files. The application was specifically designed for the lab and is available on Gur-Lab-WIS GitHub page.

Statistical Analysis. Statistical experimental details can be found in the text and in the relevant figure legends. Differences were considered significant if the $^{*}P < 0.05$, $^{**}P < 0.01$, $^{***}P < 0.001$ or $^{****}P < 0.0001$. Nonsignificant results were marked as >0.05 (ns). Two-way ANOVA, testing for genotype and batch and unpaired two-tailed Student's *t* tests were performed where appropriate to compare group means. In *SI Appendix*, Fig. S7, data from medaka were subjected to Student's *t* test, two tailed, unpaired, and the data from gecko were analyzed with two-way ANOVA followed by Tukey analysis. Tests were run using R, v. 4.4.2. Aspect ratios were compared between genotypes using a linear mixed effects model, with genotype as a fixed factor and fish ID as a random factor. Analyses were done using the "lmerTest" package in R, v. 4.5.0

Data, Materials, and Software Availability. Output of bioinformatic analysis is available as Dataset S1. RNA-seq GEO Accession number: GSE297759 (106). All other data are included in the manuscript and/or supporting information.

ACKNOWLEDGMENTS. We thank Yuval Elazari (Crown Genomics Institute, Nancy and Stephen Grand Israel National Center for Personalized Medicine, Weizmann Institute of Science) for assistance with RNA-seq data processing. We are grateful to Ziv Porat (Life Sciences Core Facilities, Weizmann Institute of Science) for his guidance in developing and optimizing the FACS protocol. We thank Neta Varsano (Department of Chemical Research Support, Weizmann Institute of Science) for her contributions to illustration and figure layout design. We also thank Ron Rotkopf (Life Sciences Core Facilities, Weizmann Institute of Science) for his support with statistical analysis and data interpretation. This work was supported by an ERC Starting Grant (Grant no: 101077470, "CRYSTALCELL") and by the Israel Science Foundation (Grant no. 691/22) awarded to D.G. Electron microscopy studies were conducted at the Irving and Cherna Moskowitz Center for Nano and Bio-Nano Imaging at the Weizmann Institute of Science. R.D. is a fellow of the Ariane de Rothschild Women Doctoral Program. Y. Barzilay is a recipient of an Azrieli Program fellowship.

Author affiliations: [a]Department of Molecular Genetics, Weizmann Institute of Science, Rehovot 7610001, Israel; [b]Department of Biomolecular Sciences, Weizmann Institute of Science, Rehovot 7610001, Israel; and [c]Department of Life Sciences Core Facilities, Weizmann Institute of Science, Rehovot 7610001, Israel

Author contributions: A.G.-A., Y. Barzilay, T.L.-G., T.O., N.M., R.D., and D.G. designed research; A.G.-A., Y. Barzilay, T.L.-G., T.O., Z.E., M.G., and N.M. performed research; T.O., Z.E., Y. Broder, N.M., R.D., M.K., and D.G. contributed new reagents/analytic tools; A.G.-A., Y. Barzilay, T.L.-G., T.O., Z.E., M.G., N.M., and D.G. analyzed data; and A.G.-A. and D.G. wrote the paper.

1. R. N. Kelsh *et al.*, Zebrafish pigmentation mutations and the processes of neural crest development. *Development* **123**, 369–389 (1996), 10.1242/dev.123.1.369.
2. J. T. Bagnara *et al.*, Common origin of pigment cells. *Science* **203**, 410–415 (1979), 10.1126/science.760198.
3. A. Ullate-Agote *et al.*, Genome mapping of a LYST mutation in corn snakes indicates that vertebrate chromatophore vesicles are lysosome-related organelles. *Proc. Natl. Acad. Sci. U.S.A.* **117**, 26307–26317 (2020), 10.1073/pnas.2003724117.
4. F. Figon, L. F. Deravi, J. Casas, Barriers and promises of the developing pigment organelle field. *Integr. Comp. Biol.* **61**, 1481–1489 (2021), 10.1093/icb/icab164.
5. J. Cunningham, C. A. MacMunn II, On the coloration of the skins of fishes, especially of pleuronectidæ. *Proc. R. Soc. Lond.* **53**, 384–388 (1893), 10.1098/rstb.1893.0010.
6. D. Gur, B. A. Palmer, S. Weiner, L. Addadi, Light manipulation by guanine crystals in organisms: Biogenic scatterers, mirrors, multilayer reflectors and photonic crystals. *Adv. Funct. Mater.* **27**, 1603514 (2017), 10.1002/adfm.201603514.
7. J. Odiorne, The occurrence of guanophores in *Fundulus*. *Proc. Natl. Acad. Sci. U.S.A.* **19**, 750–754 (1933), 10.1073/pnas.19.7.750.
8. D. Brenman-Begin *et al.*, The molecular basis of growth control in guanine crystals. *Small* **22**, e10102 (2025), https://doi.org/10.1002/smll.202510102.
9. S. T. Rohrlich, Fine structural demonstration of ordered arrays of cytoplasmic filaments in vertebrate iridophores. A comparative survey. *J. Cell Biol.* **62**, 295–304 (1974), 10.1083/jcb.62.2.295.
10. E. J. Denton, Review Lecture, On the organization of reflecting surfaces in some Marine animals. *Philos. Trans. R. Soc. Lond., Ser. B* **258**, 285–313 (1970), 10.1098/rstb.1970.0037.
11. E. J. Denton, M. Land, Mechanism of reflexion in silvery layers of fish and cephalopods. *Proc. R. Soc. Lond. B Biol. Sci.* **178**, 43–61 (1971), 10.1098/rspb.1971.0051.
12. J. N. Lythgoe, J. Shand, Changes in spectral reflexions from the iridophores of the neon tetra. *J. Physiol.* **325**, 23–34 (1982), 10.1113/jphysiol.1982.sp014132.
13. J. Teyssier, S. V. Saenko, D. van der Marel, M. C. Milinkovitch, Photonic crystals cause active colour change in chameleons. *Nat. Commun.* **6**, 6368 (2015), 10.1038/ncomms7368.
14. D. Gur *et al.*, Structural basis for the brilliant colors of the sapphirinid copepods. *J. Am. Chem. Soc.* **137**, 8408–8411 (2015), 10.1021/jacs.5b05289.
15. B. A. Palmer *et al.*, The image-forming mirror in the eye of the scallop. *Science* **358**, 1172–1175 (2017), 10.1126/science.aam9506.
16. H. N. Skold, S. Aspengren, M. Wallin, Rapid color change in fish and amphibians - function, regulation, and emerging applications. *Pigment Cell Melanoma Res.* **26**, 29–38 (2013), 10.1111/Pcmr.12040.
17. Y. Barzilay *et al.*, Specialized molecular pathways drive the formation of light-scattering assemblies in leucophores. *Proc. Natl. Acad. Sci. U.S.A.* **122**, e2424979122 (2025), 10.1073/pnas.242497912.
18. M. Land, The physics and biology of animal reflectors. *Prog. Biophys. Mol. Biol.* **24**, 75–106 (1972), 10.1016/0079-6107(72)90004-1.
19. D. Gur *et al.*, The physical and cellular mechanism of structural color change in zebrafish. *Proc. Natl. Acad. Sci. U.S.A.* **121**, e2308531121 (2024), 10.1073/pnas.2308531121.
20. F. Figon, J. Casas, Morphological and physiological colour changes in the animal kingdom. *eLS*, 1–11 (2018), 10.1002/9780470015902.a0028065.
21. D. Gur *et al.*, The mechanism of color change in the neon tetra fish: A light-induced tunable photonic crystal array. *Angew. Chem. Int. Ed.* **54**, 12426–12430 (2015), 10.1002/anie.201502268.
22. S. L. Bowman, J. Bi-Karchin, L. Le, M. S. Marks, The road to lysosome-related organelles: Insights from Hermansky-Pudlak syndrome and other rare diseases. *Traffic* **20**, 404–435 (2019), 10.1111/tra.12646.
23. L. Le, J. Sirés-Campos, G. Raposo, C. Delevoye, M. S. Marks, Melanosome biogenesis in the pigmentation of mammalian skin. *Integr. Comp. Biol.* **61**, 1517–1545 (2021), 10.1093/icb/icab078.
24. M. S. Marks, M. C. Seabra, The melanosome: Membrane dynamics in black and white. *Nat. Rev. Mol. Cell Biol.* **2**, 738–748 (2001), 10.1038/35096009.
25. G. Raposo, M. S. Marks, The dark side of lysosome-related organelles: Specialization of the endocytic pathway for melanosome biogenesis. *Traffic* **3**, 237–248 (2002), 10.1034/j.1600-0854.2002.030401.x.
26. G. Raposo, M. S. Marks, Melanosomes–dark organelles enlighten endosomal membrane transport. *Nat. Rev. Mol. Cell Biol.* **8**, 786–797 (2007), 10.1038/nrm2258.
27. Z. Eyal *et al.*, Plate-like guanine biocrystals form via templated nucleation of crystal leaflets on preassembled scaffolds. *J. Am. Chem. Soc.* **144**, 22440–22445 (2022), 10.1021/jacs.2c11136.
28. R. Deis *et al.*, Genetic control over biogenic crystal morphogenesis in zebrafish. *Nat. Chem. Biol.* **21**, 383–392 (2024), 10.1038/s41589-024-01722-1.
29. A. Wagner *et al.*, Macromolecular sheets direct the morphology and orientation of plate-like biogenic guanine crystals. *Nat. Commun.* **14**, 589 (2023), 10.1038/s41467-023-35894-6.
30. C. M. Daly, J. Willer, R. Gregg, J. M. Gross, Snow white, a zebrafish model of Hermansky-Pudlak Syndrome type 5. *Genetics* **195**, 481–494 (2013), 10.1534/genetics.113.154898.
31. E. C. Dell'Angelica, C. Mullins, S. Caplan, J. S. Bonifacino, Lysosome-related organelles. *FASEB J.* **14**, 1265–1278 (2000), 10.1096/fj.14.10.1265.
32. C. Delevoye, M. S. Marks, G. Raposo, Lysosome-related organelles as functional adaptations of the endolysosomal system. *Curr. Opin. Cell Biol.* **59**, 147–158 (2019), 10.1016/j.ceb.2019.05.003.
33. M. S. Marks, H. F. G. Heijnen, G. Raposo, Lysosome-related organelles: Unusual compartments become mainstream. *Curr. Opin. Cell Biol.* **25**, 495–505 (2013), 10.1016/j.ceb.2013.04.008.
34. L. Bento-Lopes *et al.*, Melanin's journey from melanocytes to keratinocytes: Uncovering the molecular mechanisms of melanin transfer and processing. *Int. J. Mol. Sci.* **24**, 11289 (2023), 10.3390/ijms241411289.
35. D. C. Barral *et al.*, Insights into lysosome-related organelle biogenesis: Melanosome as a model organelle. *Front. Cell Dev. Biol.* **13**, 1758081 (2026), 10.3389/fcell.2025.1758081.
36. A. Sharda, R. Flaumenhaft, The life cycle of platelet granules. *F1000Res* **7**, 236 (2018), 10.12688/f1000research.13283.1.
37. K. M. Valentijn, J. E. Sadler, J. A. Valentijn, J. Voorberg, J. Eikenboom, Functional architecture of Weibel-Palade bodies. *Blood* **117**, 5033–5043 (2011), 10.1182/blood-2010-09-267492.
38. C. Watts, Lysosomes and lysosome-related organelles in immune responses. *FEBS Open Bio.* **12**, 678–693 (2022), 10.1002/2211-5463.13388.
39. A. Sitaram, M. S. Marks, Mechanisms of protein delivery to melanosomes in pigment cells. *Physiology (Bethesda)* **27**, 85–99 (2012), 10.1152/physiol.00043.2011.
40. N. Ohbayashi, M. Fukuda, Y. Kanaho, Rab32 subfamily small GTPases: Pleiotropic Rabs in endosomal trafficking. *J. Biochem.* **162**, 65–71 (2017), 10.1093/jb/mvx027.
41. C. Wasmeier *et al.*, Rab38 and Rab32 control post-Golgi trafficking of melanogenic enzymes. *J. Cell Biol.* **175**, 271–281 (2006), 10.1083/jcb.200606050.
42. S. K. Loftus *et al.*, Mutation of melanosome protein RAB38 in chocolate mice. *Proc. Natl. Acad. Sci. U.S.A.* **99**, 4471–4476 (2002), 10.1073/pnas.072087599.
43. E. C. Dell'Angelica, The building BLOC(k)s of lysosomes and related organelles. *Curr. Opin. Cell Biol.* **16**, 458–464 (2004), 10.1016/j.ceb.2004.05.001.
44. J. J. Bultema, A. L. Ambrosio, C. L. Burek, S. M. Di Pietro, BLOC-2, AP-3, and AP-1 proteins function in concert with Rab38 and Rab32 proteins to mediate protein trafficking to lysosome-related organelles. *J. Biol. Chem.* **287**, 19550–19563 (2012), 10.1074/jbc.M112.351908.
45. S. L. Bowman *et al.*, A BLOC-1-AP-3 super-complex sorts a cis-SNARE complex into endosome-derived tubular transport carriers. *J. Cell Biol.* **220**, e202005173 (2021), 10.1083/jcb.202005173.
46. A. Sanger, J. Hirst, A. K. Davies, M. S. Robinson, Adaptor protein complexes and disease at a glance. *J. Cell Sci.* **132**, 222992 (2019), 10.1242/jcs.222992.
47. C. Delevoye *et al.*, AP-1 and KIF13A coordinate endosomal sorting and positioning during melanosome biogenesis. *J. Cell Biol.* **187**, 247–264 (2009), 10.1083/jcb.200907122.

48. A. Sitaram *et al.*, Differential recognition of a dileucine-based sorting signal by AP-1 and AP-3 reveals a requirement for both BLOC-1 and AP-3 in delivery of OCA2 to melanosomes. *Mol. Biol. Cell* **23**, 3178–3192 (2012), 10.1091/mbc.e11-06-0509.
49. J. Terglane, D. Menche, V. Gerke, Acidification of endothelial Weibel–Palade bodies is mediated by the vacuolar-type H+-ATPase. *PLoS ONE* **17**, e0270299 (2022).
50. A. L. Ambrosio, J. A. Boyle, A. E. Aradi, K. A. Christian, S. M. Di Pietro, TPC2 controls pigmentation by regulating melanosome pH and size. *Proc. Natl. Acad. Sci. U.S.A.* **113**, 5622–5627 (2016).
51. Z. Eyal *et al.*, Controlled pH alteration enables guanine accumulation and drives crystallization within iridosomes. *Nat. Chem. Biol.* **22**, 19–27 (2025), 10.1038/s41589-025-02020-0.
52. M. Huizing, A. Helip-Wooley, W. Westbroek, M. Gunay-Aygun, W. A. Gahl, Disorders of lysosome-related organelle biogenesis: Clinical and molecular genetics. *Annu. Rev. Genomics Hum. Genet.* **9**, 359–386 (2008), 10.1146/annurev.genom.9.081307.164303.
53. J. Rothkegel, S. Kaufmann, M. Wilsch-Bräuninger, C. Lopes, R. Mateus, Purine molecular interactions determine anisotropic shape of zebrafish biogenic crystals. *Small Methods* **9**, e01956 (2025), 10.1002/smtd.202401956.
54. N. Oshima, A. Kasai, Iridophores involved in generation of skin color in the zebrafish. *Brachydanio rerio*. *Forma Tokyo* **17**, 91–101 (2002).
55. D. Gur *et al.*, In situ differentiation of iridophore crystallotypes underlies zebrafish stripe patterning. *Nat. Commun.* **11**, 6391 (2020), 10.1038/s41467-020-20088-1.
56. A. Ullate-Agote, A. C. Tzika, The dynamic behavior of chromatophores marks the transition from bands to spots in leopard geckos. *Proc. Natl. Acad. Sci. U.S.A.* **121**, e2400486121 (2024), 10.1073/pnas.2400486121.
57. M. Hirata, K.-I. Nakamura, T. Kanemaru, Y. Shibata, S. Kondo, Pigment cell organization in the hypodermis of zebrafish. *Dev. Dyn.* **227**, 497–503 (2003), 10.1002/dvdy.10334.
58. A. P. Singh, U. Schach, C. Nusslein-Volhard, Proliferation, dispersal and patterned aggregation of iridophores in the skin prefigure striped colouration of zebrafish. *Nat. Cell Biol.* **16**, 607–614 (2014), 10.1038/ncb2955.
59. D. Gur *et al.*, The dual functional reflecting iris of the zebrafish. *Adv. Sci.* **5**, 1800338 (2018), 10.1002/advs.201800338.
60. P. Salis *et al.*, Developmental and comparative transcriptomic identification of iridophore contribution to white barring in clownfish. *Pigment Cell Melanoma Res.* **32**, 391–402 (2019), 10.1111/pcmr.12766.
61. V. M. Lewis *et al.*, Fate plasticity and reprogramming in genetically distinct populations of *Danio leucophores*. *Proc. Natl. Acad. Sci. U.S.A.* **116**, 11806–11811 (2019), 10.1073/pnas.1901021116.
62. K. Petratou *et al.*, A systems biology approach uncovers the core gene regulatory network governing iridophore fate choice from the neural crest. *PLoS Genet.* **14**, e1007402 (2018), 10.1371/journal.pgen.1007402.
63. M. Hirata, K. Nakamura, S. Kondo, Pigment cell distributions in different tissues of the zebrafish, with special reference to the striped pigment pattern. *Dev. Dyn.* **234**, 293–300 (2005), 10.1002/dvdy.20513.
64. C. W. Higdon, R. D. Mitra, S. L. Johnson, Gene expression analysis of zebrafish melanocytes, iridophores, and retinal pigmented epithelium reveals indicators of biological function and developmental origin. *PLoS ONE* **8**, e67801 (2013), 10.1371/journal.pone.0067801.
65. Y. Li *et al.*, Integrative analysis of circadian transcriptome and metabolic network reveals the role of de novo purine synthesis in circadian control of cell cycle. *PLoS Comput. Biol.* **11**, e1004086 (2015), 10.1371/journal.pcbi.1004086.
66. T. Subkhankulova *et al.*, Zebrafish pigment cells develop directly from persistent highly multipotent progenitors. *Nat. Commun.* **14**, 1258 (2023), 10.1038/s41467-023-36876-4.
67. J. A. Lister, B. M. Lane, A. Nguyen, K. Lunney, Embryonic expression of zebrafish MiT family genes tfe3b, tfeb, and tfec. *Dev. Dyn.* **240**, 2529–2538 (2011), 10.1002/dvdy.22743.
68. L. M. Saunders *et al.*, Thyroid hormone regulates distinct paths to maturation in pigment cell lineages. *Elife* **8**, e45181 (2019), 10.7554/eLife.45181.
69. Y. Zhou *et al.*, Metascape provides a biologist-oriented resource for the analysis of systems-level datasets. *Nat. Commun.* **10**, 1523 (2019), 10.1038/s41467-019-09234-6.
70. D. Szklarczyk *et al.*, The STRING database in 2023: Protein-protein association networks and functional enrichment analyses for any sequenced genome of interest. *Nucleic Acids Res.* **51**, D638–d646 (2023), 10.1093/nar/gkac1000.
71. P. Shannon *et al.*, Cytoscape: A software environment for integrated models of biomolecular interaction networks. *Genome Res.* **13**, 2498–2504 (2003), 10.1101/gr.1239303.
72. S. Y. Park, X. Guo, Adaptor protein complexes and intracellular transport. *Biosci. Rep.* **34**, e00123 (2014), 10.1042/bsr20140069.
73. J. Shin, A. Nile, J. W. Oh, Role of adaptin protein complexes in intracellular trafficking and their impact on diseases. *Bioengineered* **12**, 8259–8278 (2021), 10.1080/21655979.2021.1982846.
74. C. M. Dooley *et al.*, Slc45a2 and V-ATPase are regulators of melanosomal pH homeostasis in zebrafish, providing a mechanism for human pigment evolution and disease. *Pigment Cell Melanoma Res.* **26**, 205–217 (2013), 10.1111/pcmr.12053.
75. K. J. More, J. G. G. Kaufman, J. B. Dacks, P. T. Manna, Evolutionary origins of the lysosome-related organelle sorting machinery reveal ancient homology in post-endosome trafficking pathways. *Proc. Natl. Acad. Sci. U.S.A.* **121**, e2403601121 (2024), 10.1073/pnas.2403601121.
76. M. Starcevic, E. C. Dell'Angelica, Identification of snapin and three novel proteins (BLOS1, BLOS2, and BLOS3/Reduced pigmentation) as subunits of biogenesis of lysosome-related organelles complex-1 (BLOC-1). *J. Biol. Chem.* **279**, 28393–28401 (2004), 10.1074/jbc.M402513200.
77. X. Wu, F. Wang, K. Rao, J. R. Sellers, J. A. Hammer, Rab27a is an essential component of melanosome receptor for myosin Va. *Mol. Biol. Cell* **13**, 1735–1749 (2002), 10.1091/mbc.01-12-0595.
78. I. J. McGough *et al.*, Identification of molecular heterogeneity in SNX27–retromer–mediated endosome-to-plasma-membrane recycling. *J. Cell Sci.* **127**, 4940–4953 (2014), 10.1242/jcs.156299.
79. Z. Ma, M. N. Islam, T. Xu, E. Song, AP-3 adaptor complex-mediated vesicle trafficking. *Biophys. Rep.* **7**, 91–100 (2021), 10.52601/bpr.2021.200051.
80. M. Huizing *et al.*, AP-3 mediates tyrosinase but not TRP-1 trafficking in human melanocytes. *Mol. Biol. Cell* **12**, 2075–2085 (2001), 10.1091/mbc.12.7.2075.
81. K. Newell-Litwa, E. Seong, M. Burmeister, V. Faundez, Neuronal and non-neuronal functions of the AP-3 sorting machinery. *J. Cell Sci.* **120**, 531–541 (2007), 10.1242/jcs.03365.
82. P. Kantheti *et al.*, Mutation in AP-3 delta in the mocha mouse links endosomal transport to storage deficiency in platelets, melanosomes, and synaptic vesicles. *Neuron* **21**, 111–122 (1998), 10.1016/s0896-6273(00)80519-x.
83. L. Feng *et al.*, The beta3A subunit gene (Ap3b1) of the AP-3 adaptor complex is altered in the mouse hypopigmentation mutant pearl, a model for Hermansky-Pudlak syndrome and night blindness. *Hum. Mol. Genet.* **8**, 323–330 (1999), 10.1093/hmg/8.2.323.
84. U. Coppola, G. Annona, S. D'Aniello, F. Ristoratore, Rab32 and Rab38 genes in chordate pigmentation: An evolutionary perspective. *BMC Evol. Biol.* **16**, 26 (2016), 10.1186/s12862-016-0596-1.
85. S. M. Di Pietro, J. M. Falcón-Pérez, E. C. Dell'Angelica, Characterization of BLOC-2, a complex containing the Hermansky-Pudlak syndrome proteins HPS3, HPS5 and HPS6. *Traffic* **5**, 276–283 (2004), 10.1111/j.1600-0854.2004.0171.x.
86. J. Lee, N. M. G. Dieckmann, J. R. Edgar, G. M. Griffiths, R. M. Siegel, Fas ligand localizes to intraluminal vesicles within NK cell cytolytic granules and is enriched at the immune synapse. *Immun. Inflamm. Dis.* **6**, 312–321 (2018), 10.1002/iid3.219.
87. A. C. Theos *et al.*, A lumenal domain-dependent pathway for sorting to intralumenal vesicles of multivesicular endosomes involved in organelle morphogenesis. *Dev. Cell* **10**, 343–354 (2006), 10.1016/j.devcel.2006.01.012.
88. G. Niel *et al.*, The tetraspanin CD63 regulates ESCRT-independent and -dependent endosomal sorting during melanogenesis. *Dev. Cell* **21**, 708–721 (2011), 10.1016/j.devcel.2011.08.019.
89. A. C. Theos *et al.*, Functions of adaptor protein (AP)-3 and AP-1 in tyrosinase sorting from endosomes to melanosomes. *Mol. Biol. Cell* **16**, 5356–5372 (2005), 10.1091/mbc.e05-07-0626.
90. M. Fukuda, Rab GTPases: Key players in melanosome biogenesis, transport, and transfer. *Pigment Cell Melanoma Res.* **34**, 222–235 (2021), 10.1111/pcmr.12931.
91. A. Helip-Wooley *et al.*, Improper trafficking of melanocyte-specific proteins in Hermansky-Pudlak syndrome type-5. *J. Invest. Dermatol.* **127**, 1471–1478 (2007). 10.1038/sj.jid.5700737.
92. B. Watt, G. van Niel, G. Raposo, M. S. Marks, PMEL: A pigment cell-specific model for functional amyloid formation. *Pigment Cell Melanoma Res.* **26**, 300–315 (2013), 10.1111/pcmr.12067.
93. F. G. Canovas, F. Garcia-Carmona, J. V. Sanchez, J. L. Pastor, J. A. Teruel, The role of pH in the melanin biosynthesis pathway. *J. Biol. Chem.* **257**, 8738–8744 (1982), 10.1016/S0021-9258(18)34190-5.
94. A. Wagner *et al.*, The non-classical crystallization mechanism of a composite biogenic guanine crystal. *Adv. Mater.* **34**, e2202242 (2022), 10.1002/adma.202202242.
95. S. Kumar *et al.*, TimeTree 5: An expanded resource for species divergence times. *Mol. Biol. Evol.* **39**, msac174 (2022), 10.1093/molbev/msac174.
96. M. P. Levesque, J. Krauss, C. Koehler, C. Boden, M. P. Harris, New tools for the identification of developmentally regulated enhancer regions in embryonic and adult zebrafish. *Zebrafish* **10**, 21–29 (2013), 10.1089/zeb.2012.0775.
97. D. A. Jaitin *et al.*, Massively parallel single-cell RNA-seq for marker-free decomposition of tissues into cell types. *Science* **343**, 776–779 (2014), 10.1126/science.1247651.
98. H. Keren-Shaul *et al.*, MARS-seq2.0: An experimental and analytical pipeline for indexed sorting combined with single-cell RNA sequencing. *Nat. Protoc.* **14**, 1841–1862 (2019), 10.1038/s41596-019-0164-4.
99. J. Lindner *et al.*, UTAP2: An enhanced user-friendly transcriptome and epigenome analysis pipeline. *BMC Bioinformatics* **26**, 79 (2025), 10.1186/s12859-025-06090-8.
100. M. V. Kuleshov *et al.*, Enrichr: A comprehensive gene set enrichment analysis web server 2016 update. *Nucleic Acids Res.* **44**, W90–W97 (2016), 10.1093/nar/gkw377.
101. A. M. Newman *et al.*, Determining cell type abundance and expression from bulk tissues with digital cytometry. *Nat. Biotechnol.* **37**, 773–782 (2019), 10.1038/s41587-019-0114-2.
102. A. Sur *et al.*, Single-cell analysis of shared signatures and transcriptional diversity during zebrafish development. *Dev. Cell* **58**, 3028.e12–3047.e12 (2023), 10.1016/j.devcel.2023.11.001.
103. F. Kroll *et al.*, A simple and effective F0 knockout method for rapid screening of behaviour and other complex phenotypes. *Elife* **10**, e59683 (2021), 10.7554/eLife.59683.
104. D. M. Parichy, M. R. Elizondo, M. G. Mills, T. N. Gordon, R. E. Engeszer, Normal table of postembryonic zebrafish development: Staging by externally visible anatomy of the living fish. *Dev. Dyn.* **238**, 2975–3015 (2009), 10.1002/dvdy.22113.
105. J. R. Kremer, D. N. Mastronarde, J. R. McIntosh, Computer visualization of three-dimensional image data using IMOD. *J. Struct. Biol.* **116**, 71–76 (1996), 10.1006/jsbi.1996.0013.
106. A. Gorelick-Ashkenazi *et al.*, Data from "Lysosome-Related Organelles Orchestrate Biogenic Crystal Formation in Pigment Cells". NCBI GEO. https://www.ncbi.nlm.nih.gov/geo/query/acc.cgi?acc=GSE297759. Deposited 21 May 2025.